A discrete network model for bond failure and frictional sliding in fibrous materials

D.V. Wilbrink, L.A.A. Beex, R.H.J. Peerlings *

Department of Mechanical Engineering, Eindhoven University of Technology, P.O. Box 513, 5600 MB Eindhoven, The Netherlands

ABSTRACT

Discrete network models and lattice models using trusses or beams can be used to mechanically model fibrous materials, since the discrete elements represent the individual fibers or yarns at the mesoscale of these materials. Consequently, local mesoscale phenomena, such as individual fiber failure and interfiber bond failure, can be incorporated. Only a few discrete network models in which bond failure is incorporated include frictional fiber sliding that occurs after bond failure has taken place, although this occurs in the mechanical behaviour of several fibrous materials. In this paper, a spring network model for interfiber bond failure and subsequent frictional fiber sliding is developed, which is formulated in a thermodynamical setting. The thermodynamical basis ensures that performed mechanical work is either stored in the network or dissipated due to bond failure and subsequent sliding. A numerical implementation of the framework is proposed in which the kinematic and internal variables are simultaneously solved, because the internal variables are directly coupled in the framework. Variations in network connectivity, bond strength, fiber length and anisotropy are implemented in the framework. The results show amongst others that the macroscopic yield point scales with the bond strength and that the macroscopic stiffness and the macroscopic yield point scale with the fiber length. The presented results also show that the macroscopic yield point becomes significantly less pronounced for an increase of the fiber length.

© 2013 Elsevier Ltd. All rights reserved.

1. Introduction

In the discrete modelling of materials, lattice models and network models, as for instance shown in Fig. 1, have received considerable attention over the past decades. They have been used for the mechanical modelling of materials at various length scales (Herrmann and Roux, 1990; Ostoja-Starzewski, 2002; Hatami-Marbini and Picu, 2009; Hatami-Marbini et al., 2013). The system of discrete elements and nodes allows a discrete representation of a material's microstructure and heterogeneity (Ostoja-Starzewski, 2002; Lilliu and Van Mier, 2003; Ridruejo et al., 2012). Hence, discrete networks have been applied to model various materials with a distinctively heterogenous microstructure, e.g., concrete (Schlangen and Van, 1992; Lilliu and Van Mier, 2003), composites (Arnoux et al., 2002; Bolander and Sukumar, 2005) and a variety of fibrous materials (Alava and Duxbury, 1996; Raïsänen et al., 1997; Heyden, 2000; Boubaker et al., 2007; Potluri and Manan, 2007; Ridruejo et al., 2010).

Fibrous materials are of particular interest in the present study. Their discrete fibers at the mesoscale can be captured individually by the discrete elements of network models. The failure process, that underlies the limiting mechanical properties, is governed by a combination of mechanical mesoscale phenomena. Examples are fiber bending, stretching and failure, as well as the loss of interfiber connectivity (Isaksson and Hägglund, 2007), sliding friction and pullout (Niskanen, 1998; Ridruejo et al., 2010, 2011). To what extent each of these mechanisms contributes to failure, depends on the material of interest and can be complex to assess with experimental techniques. Network models however can be used to asses and investigate these mechanisms and several of these models can be found in the literature. Some illustrative examples are highlighted below, where a distinction is made between the constitutive behaviour of the elements and that of the nodes.

The simplest element behaviour assumed in the literature is elastic (Heyden, 2000; Ridruejo et al., 2010). To simulate fiber failure in fibrous materials however, various network models allow the elements to fail in a brittle manner when subjected to specific loading conditions (Curtin and Scher, 1989; Heyden, 2000). Since the fibers in many of these materials exhibit plastic behaviour before failure (Page and El-Hosseiny, 1983; Niskanen, 1998; Isaksson et al., 2006), preference may be given to elastoplastic element behaviour. This is for instance done in a pin-jointed model to simulate the tensile behaviour of paper (Bronkhorst, 2003).

The simplest way to connect the elements is by pin-jointed nodes. This however implies a perfect bonding, i.e., no bond failure, which can be a reason that several network models do not capture experimentally observed responses accurately. Bronkhorst (2003) for instance, suggests that incorporating interfiber bond failure may improve the response of his network model for paper.

* Corresponding author. Tel.: +31 40 247 2788.
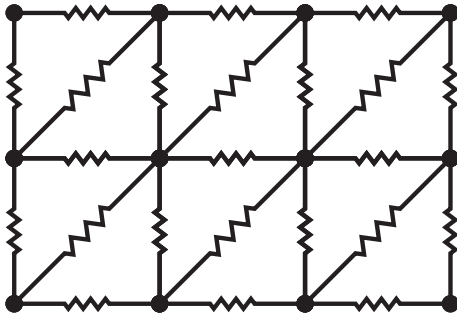 E-mail address: r.h.j.peerlings@tue.nl (R.H.J. Peerlings).

Fig. 1. Example of a simple discrete network, a periodic (triangular) spring network, in which elements (springs) are connected at nodes.

Furthermore, some experimental studies have shown that the degradation of interfiber connectivity plays a role in the deformation process of various fibrous materials (Isaksson et al., 2006; Zhu et al., 2007; Ridruejo et al., 2010, 2011; Kulachenko and Uesaka, 2012).

A number of bond models have been proposed in literature to account for the loss of interfiber connectivity. An example is a linear-brittle bond model (Delaplace et al., 1996; Ridruejo et al., 2010). In another network connectivity model for cellulose fiber fluff, each bond is modelled using a number of elastic elements. Each element may fail under influence of mechanical loading, leading to a stepwise strength decay until complete failure (Heyden, 2000). Discrepancies with realistic behaviour appear to stem from both the absence of interfiber frictional sliding after bond failure has taken place and the energy dissipation associated with it.

Recently, models have been proposed by Ridruejo et al. (2010, 2011) and Kulachenko and Uesaka (2012) to account for the effects of interfiber frictional sliding after bond failure has occurred. Kulachenko and Uesaka (2012) have used their model to predict interfiber bond failure in a disordered fiber network. Subsequent frictional fiber sliding is introduced by the use of a Coulomb friction model for the bonds. In the model of Ridruejo et al. (2010), which is used to simulate the in-plane mechanical behaviour of glass fiber nonwoven materials, the normal force has a bilinear decay as a function of the sliding distance. Compared to a linear, brittle bond model, the frictional bond model (with a fitting procedure for the normal load's bilinear decay) is proven to be in better agreement with the gradual loss of load-carrying capacity witnessed in tensile experiments. This is explained by its ability to dissipate energy in the bonds.

Based on literature, it appears that frictional fiber sliding subsequent to bond failure is a key aspect in the accurate network modelling of the mechanical behaviour of many fibrous materials if one desires to describe the mechanical response until complete failure. Whereas a variety of other mesomechanical features have been dealt with in the literature, discrete models that include bond failure as well as subsequent frictional fiber sliding are relatively scarce.

The objective of the present paper is to incorporate interfiber bond failure and the subsequent frictional fiber sliding in a thermodynamically consistent spring network model. The mesoscopic network model is proposed such that the influence of a number of mesoscopic parameters can systematically be studied.

A numerical modelling framework is proposed to this end, which is based on the thermodynamical formulation of a network model. The (isothermal) thermodynamical formulation is similar to those used for continuum mechanics (Germain, 1973). However, the formulations of the stored energy and the dissipation potential are specifically derived for the spring network model with bond failure and subsequent frictional fiber sliding. In the present study,

the formulation of the stored energy only allows for small sliding displacements. A Coulomb-like friction law is used in the dissipation potential for the fiber-bond behaviour, in which the maximum friction force is constant. This entails that the force at which bond failure takes place is the same as the force necessary to accommodate subsequent sliding. However, the dissipation potential can be altered so that different bond descriptions can be incorporated.

This paper consists of three parts. The first part details the model by deriving the equations that govern the mechanical deformation of discrete dissipative systems. This theory is applied to spring network models that represent fibrous structures with linear elastic elements and Coulomb nodal friction to capture dry interfiber contact. The second part proposes an algorithm that is capable of numerically approximating the model. This algorithm uses Newton–Raphson iterations to solve the nonlinear equations which govern equilibrium, and employs an active set strategy to distinguish between active sliding and static friction. The third part explores the macroscopic response of the model for a rather straightforward spring network; a periodic X-braced spring network. The resulting macroscopic response has many features of elastoplasticity. The influence of several mesoscopic parameters, such as bond strength and fiber length, is investigated using the model.

The following notation is used throughout this paper. Matrices, including column matrices, are denoted by bold letters. Subscripts denote the components of column matrices and matrices. Quantities x_i (where $i = 1, \ldots, n$) are stored in a column matrix $\mathbf{x}$ and quantities A_{ij} (where $i = 1, \ldots, n$ and $j = 1, \ldots, m$) are stored in matrix $\mathbf{A}$ of size $n \times m$. Inequalities of column matrices apply to each of their individual components, e.g., $\mathbf{x} \leqslant \mathbf{y}$ is equivalent to $x_i \leqslant y_i$ for all $i = 1, \ldots, n$. An element-wise multiplication $\mathbf{x} * \mathbf{y} = \mathbf{z}$ results in $z_i = x_i y_i$ for all $i = 1, \ldots, n$.

2. Modelling

The objective of the following development is to formulate the thermodynamical setting that describes the deformation of a spring network which may dissipate energy. The first part of the thermodynamical setting is similar to those that are regularly used for (isothermal) continuum models (Germain, 1973) and results in a model that includes dissipation, for instance by plasticity, damage or friction. The theory is afterwards specifically developed for spring network models with nodal friction, by deriving formulations for the stored energy and the dissipation potential.

2.1. Governing equations for a dissipative system

Here we derive the governing equations of (isothermal) mechanical models on a thermodynamical basis, along the lines of Germain (1973). The system is characterized by (controllable) kinematic variables (degrees of freedom), that are stored in column matrix $\mathbf{u}$, and (uncontrollable) internal variables, that are stored in column matrix $\mathbf{s}$. The kinematic variables $\mathbf{u}$ include the displacements of the nodes in the network, but may also include additional kinematic quantities, such as rotations if a beam network is considered. The total rate of work of the system, the internal power P_{int}, is the sum of the work performed by internal forces, present in column matrix $\mathbf{F}_u$, that are associated with the rate of the kinematic variables $\mathbf{u}$, i.e.,

$$P_{int} = \dot{\mathbf{u}}^T \mathbf{F}_u. \tag{1}$$

The forces $\mathbf{F}_u$ may be accompanied by externally imposed forces, $\mathbf{F}_{ext}$, such that the external power of the system, P_{ext}, can be written as:

$$P_{ext} = \dot{\mathbf{u}}^T \mathbf{F}_{ext}. \tag{2}$$

The principle of virtual power dictates that in static equilibrium, we have for arbitrary (virtual) velocities:

$$P_{int} = P_{ext} \quad \forall \dot{\mathbf{u}}. \tag{3}$$

An implication of this so-called virtual-power-statement (using Eqs. (1) and (2)) is that

$$\mathbf{F}_u = \mathbf{F}_{ext}. \tag{4}$$

This equation may be recognized as static equilibrium, i.e., each of its components expresses the force equilibrium in a particular node in a certain direction.

The energy stored in the model is a function of the sets of kinematic variables $\mathbf{u}$ and internal variables $\mathbf{s}$. Consequently, the rate of internal (elastic) energy $\dot{E}$ can be written as:

$$\dot{E} = \dot{\mathbf{u}}^T \frac{\partial E}{\partial \mathbf{u}} + \dot{\mathbf{s}}^T \frac{\partial E}{\partial \mathbf{s}}. \tag{5}$$

The first law of thermodynamics dictates that energy can neither be created nor destroyed. This implies that the rate of dissipation $\dot{D}$ can be expressed as $\dot{D} = P_{int} - \dot{E}$. By substitution of Eqs. (1) and (5) in this expression, the dissipation rate $\dot{D}$ can be expressed as:

$$\dot{D} = \dot{\mathbf{u}}^T \left(\mathbf{F}_u - \frac{\partial E}{\partial \mathbf{u}} \right) - \dot{\mathbf{s}}^T \frac{\partial E}{\partial \mathbf{s}}. \tag{6}$$

It is now assumed that all dissipative processes are characterized by $\mathbf{s}$; hence, no dissipation occurs for constant $\mathbf{s}$. This can be satisfied for arbitrary $\dot{\mathbf{u}}$ by defining the forces $\mathbf{F}_u$ as:

$$\mathbf{F}_u = \frac{\partial E}{\partial \mathbf{u}}. \tag{7}$$

Furthermore, we define a column matrix with dissipation forces, $\mathbf{F}_s$, as the derivatives of the stored energy with respect to the internal variables as:

$$\mathbf{F}_s = -\frac{\partial E}{\partial \mathbf{s}}, \tag{8}$$

such that by substituting Eqs. (7) and (8) in Eq. (6), the dissipation rate can be expressed as

$$\dot{D} = \dot{\mathbf{s}}^T \mathbf{F}_s. \tag{9}$$

The second law of thermodynamics dictates that dissipation is irreversible, such that

$$\dot{D} \geqslant 0. \tag{10}$$

The evolution of the internal variables $\mathbf{s}$ must be such that this condition (in Eq. (10)) is satisfied. Given the fact that the forces $\mathbf{F}_s$ are energetically conjugate to $\dot{\mathbf{s}}$, it is natural to define the evolution of $\mathbf{s}$ in terms of $\mathbf{F}_s$, taking into account the constraint imposed by Eqs. (9) and (10).

2.2. Application: network of elastic springs with dry nodal friction

The relations derived above are now applied to a rate-independent planar network model of springs that includes interfiber bond failure and subsequent frictional fiber sliding using a Coulomb friction model.

If it is assumed that the network model represents a fictitious fibrous material for which fiber bending can be ignored (although this is important for several fibrous materials), chains of elements in the network can be considered as fibers (or fiber bundles). Hence, each element represents a fiber segment. This is illustrated in the left image of Fig. 2, in which element e between nodes A and B is a segment of the fiber that is marked by the dashed gray line in the undeformed configuration. Fibers are connected to other fibers in nodes. Nodes allow multiple fibers to interact in one point, as shown in the right image of Fig. 2. The kinematic variables $\mathbf{u}$ are defined as the set of nodal displacements in space; they are used to formulate a set of vectors that describe the nodal displacements (e.g., $\vec{u}_A$ and $\vec{u}_B$ in the left image of Fig. 2).

Fibers and nodes can be viewed as separate bodies and fibers may slide with respect to the nodes. Note that fiber sliding with respect to a node changes the length of the fiber's segments adjacent to the node and thus lets the spring force increase in one of the fiber's elements and decrease in another. However, fibers connected in a node initially stay connected in that node at all times. For the ith fiber-node interaction, the amount of sliding is characterized by the fiber's axial sliding displacement, s_i, relative to the node. The fact that the sliding displacement is a scalar (its direction is governed by the local fiber orientation as Fig. 2 shows), implies that it retains its validity regardless of a possible change of direction of the fiber in a node. As a node includes the interaction of a number of fibers, multiple internal variables may be associated with each node - one for each fiber. The column matrix $\mathbf{s}$ comprises all sliding displacements s_i of all nodes. Free fiber ends are assumed to be always sufficiently long so that pull-out never occurs, i.e., fibers and nodes remain in contact at all times.

As Eqs. (7) and (8) show, a key factor in the model is the system energy E. The system energy may have a nonlinear dependence on the variables $\mathbf{u}$ and $\mathbf{s}$. For a network with n_e elastic springs where the eth element ($e = 1, \ldots, n_e$) has constant stiffness, k_e, and an equivalent elongation, ω_e, the system energy can be expressed as follows:

$$E(\mathbf{u}, \mathbf{s}) = \sum_{e=1}^{n_e} E_e(\mathbf{u}, \mathbf{s}) = \sum_{e=1}^{n_e} \frac{1}{2} k_e \omega_e^2, \tag{11}$$

with

$$\omega_e = \|\vec{x}_B + \vec{u}_B - \vec{x}_A - \vec{u}_A\| - \|\vec{x}_B - \vec{x}_A\| + s_B - s_A. \tag{12}$$

Here, $\vec{x}_A$ and $\vec{x}_B$ are the position vectors of nodes A and B, respectively, to which the element is attached (see Fig. 2). This definition allows large rotations, but no large sliding displacements, since they do not influence the stiffness, k_e. As a result, the effect of fiber slid-
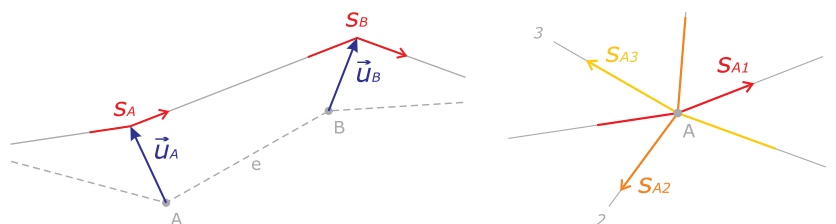

Fig. 2. Illustration of the variables of the spring network with dry interfiber friction. (Left) element e between nodes A and B is part of a fiber (dashed in the undeformed configuration and solid in the deformed configuration). The nodes are displaced in space (characterized by $\vec{u}_A$ and $\vec{u}_B$) and the fiber may slide through both nodes by distances s_A and s_B. (Right) in node A, three fibers are linked together, each has its own sliding displacement through this node.

ing on E with respect to a node is equivalent to the displacement of that node in fiber direction for a one dimensional chain of elements.

For the node-fiber behaviour, the choice is made to use a constant friction resistance. This entails that the static friction force and dynamic friction force are constant and equal to each other for every fiber-node interaction. This corresponds to a Coulomb friction model with a constant normal force. The sliding displacement s_i for the ith fiber-node interaction is assumed to depend on the force F_{si} (i.e., the ith component of $\mathbf{F}_s$) associated with this interaction. In the following discussion of an individual fiber-node interaction, the subscripts i are dropped for convenience, except for cases where this conflicts with previous definitions.

Sliding may occur if the magnitude of the driving force F_s exceeds the critical sliding force $F_{sc} > 0$, which quantifies the friction resistance. We assume F_{sc} to be a constant here, i.e., the static and dynamic friction force are equal and the latter does not depend on the amount of sliding. However, the extension of the present framework to cases where e.g., the dynamic friction force is considerably lower than the static friction force (or bond strength) is relatively straightforward. Similarly, we adopt a rate-independent formulation here, but this may be extended to rate-dependent sliding along the same lines.

A loading function, ϕ, is defined according to:

$$\phi = |F_s| - F_{sc}, \tag{13}$$

using which the sliding criterion can be formulated as $\phi = 0$. The sliding velocity is described using a monotonically increasing Lagrange multiplier ξ:

$$\dot{s} = \dot{\xi} \frac{\partial \phi}{\partial F_s} = \dot{\xi} \, \text{sign}(F_s). \tag{14}$$

In case the sliding criterion $\phi = 0$ is met, a change of ξ prevents the sliding force F_s from exceeding its limit F_{sc}, i.e., to maintain $\phi \leqslant 0$ at all times. If the criterion is not met, the driving force F_s is insufficient to induce sliding, hence, $\dot{\xi} = 0$. These conditions are mathematically expressed by the following so-called Kuhn–Tucker (KT) conditions:

$$\phi\dot{\xi} = 0 \quad \phi \leqslant 0 \quad \dot{\xi} \geqslant 0. \tag{15}$$

Note that since $\text{sign}(\dot{s}) = \text{sign}(F_s)$, the irreversibility requirement for dissipation is satisfied component-wise (i.e., $\dot{D}_i = \dot{s}_i F_{si} \geqslant 0$) and therefore also for the entire network.

The present model shows similarities with conventional, rate-independent elastoplasticity models, which are also governed by equilibrium and plasticity laws and characterized by sets of kinematic and internal variables. A substantial difference with these models is that in the present model, the sliding displacement s_i in the ith fiber-node connection depends on F_{si} (through the loading function ϕ_i), which is a function of several sliding displacements, present in $\mathbf{s}$, through Eqs. (8), (11) and (12). This renders the plasticity (the sliding displacements) in the present model intrinsically nonlocal, whereas in conventional elastoplasticity problems these quantities are governed locally and are merely indirectly coupled through the equilibrium equations.

3. Numerical implementation

3.1. Incremental-iterative procedure

For the numerical implementation, we consider that the network model is deformed sufficiently slowly so that a quasi-static analysis suffices. The loading process is divided into time increments Δt, where Δ refers to an incremental change. At time t, the entire solution is known and characterized by displacements $\mathbf{u}^{(t)}$ and sliding displacements $\mathbf{s}^{(t)}$. From time t to time $t + \Delta t$, addi-

tional external forces and/or displacements may be imposed, under which equilibrium is to be regained at time $t + \Delta t$. For time $t + \Delta t$, we wish to determine the displacement solution; i.e., all nodal displacements $\mathbf{u}$ and sliding displacements $\mathbf{s}$, where the superscript, $t + \Delta t$, is dropped for ease of notation. The following discusses the solution procedure for one increment; this procedure is repeated for each new increment to obtain the solution for the entire time interval considered.

As was shown in the model derivation, equilibrium dictates that the forces that correspond to the displacement solution must obey the following conditions at time $t + \Delta t$. First, the force equilibrium in Eq. (4) must be satisfied. Second, the KT-conditions in Eq. (15), dictated by the Coulomb friction model, must be obeyed. These are formulated for the entire system as follows:

$$\boldsymbol{\phi} * \dot{\boldsymbol{\xi}} = 0 \quad \boldsymbol{\phi} \leqslant \mathbf{0} \quad \dot{\boldsymbol{\xi}} \geqslant \mathbf{0}. \tag{16}$$

Eq. (4) as well as Eq. (16) have a nonlinear dependence on the variables $\mathbf{u}$ and $\mathbf{s}$, due to the formulation of the elastic energy E in Eqs. (11) and (12). Consequently, an iterative solution procedure is used within every increment.

As a consequence of the intrinsically nonlocal plasticity in the present model, the elastic predictor-plastic corrector algorithms, e.g., Simo and Taylor (1986), that are commonly used to solve elastoplastic problems are not usable. The problem outlined above shows similarities with nonlinear programming problems in constrained optimization, for which a range of solution algorithms may be employed, such as an augmented Lagrangian formulation (Heegaard and Curnier, 1993).

Here, the choice is made for the Newton–Raphson method in which the nonlinear governing equations are solved iteratively, since it allows for quadratic convergence. Because of the method's limited robustness, small incremental loading steps are required. This method is combined with an active set strategy to deal with the inequality constraints imposed by the Coulomb friction model.

This solution procedure is similar to the generalized reduced gradient (GRG) method, first proposed by Abadie and Carpentier (1969). Both the GRG and the present method rely on linearization of the governing equations. Rather than explicitly formulating the reduced gradient, performing a line search in its direction and subsequently restoring the state variables, as in the GRG method, one linear system is formulated and solved in the present method. This allows for applying indirect solution methods rather than explicitly determining large inverse matrices, which is computationally more efficient for large systems (containing hundreds of nodes or more).

3.2. Linearization

The following discusses the linearization for one Newton–Raphson iteration. Boundary conditions and variations in sliding activity are treated separately below. For the moment these are left out of consideration, such that $\mathbf{u}$ and $\mathbf{s}$ can be changed freely. For now, it is also assumed that all sliders are active, i.e., $\boldsymbol{\phi} = \mathbf{0}$, which is equivalent to $|\mathbf{F}_s| = \mathbf{F}_{sc}$ due to Eq. (13). The forces $\mathbf{F}_u$ and $\mathbf{F}_s$ both depend on $\mathbf{u}$ and $\mathbf{s}$, such that the linearized iterative force changes $\delta\mathbf{F}_u$ and $\delta\mathbf{F}_s$ may be expressed as:

$$\delta\mathbf{F}_u = \mathbf{K}_{uu}\delta\mathbf{u} + \mathbf{K}_{us}\delta\mathbf{s},$$

$$\delta\mathbf{F}_s = \mathbf{K}_{su}\delta\mathbf{u} + \mathbf{K}_{ss}\delta\mathbf{s}, \tag{17}$$

where δ indicates an iterative change. The tangent matrices of the form $\mathbf{K}_{pq}$ are found by differentiating E with respect to both variables denoted in the subscript, e.g.:

$$\mathbf{K}_{us} = \frac{\partial\mathbf{F}_u}{\partial\mathbf{s}} = \frac{\partial^2 E}{\partial\mathbf{s}\partial\mathbf{u}}. \tag{18}$$

More precisely, the components of this matrix $\mathbf{K}_{us}$ are given by:

$$(K_{us})_{ij} = \frac{\partial^2 E}{\partial s_j \partial u_i} \tag{19}$$

where i and j run over all components of $\mathbf{u}$ and $\mathbf{s}$ respectively.

Boundary conditions are applied to particular nodes. Since external forces are already incorporated in column matrix $\mathbf{F}_{ext}$, the boundary conditions discussed here are solely displacement constraints. Since $\mathbf{s}$ contains internal variables that cannot be controlled, constraints only act on a part of the kinematic variables $\mathbf{u}$. Hence, a distinction is made between the constrained displacements, indicated with subscript c, and the other, 'free' displacements, with subscript f. The constrained displacements are kept constant during all but the first iteration of every increment, such that $\delta\mathbf{u}_c = \mathbf{0}$. The displacement correction $\delta\mathbf{u}$ can thus be written as:

$$\delta\mathbf{u} = \begin{pmatrix} \delta\mathbf{u}_f \\ \delta\mathbf{u}_c \end{pmatrix} = \begin{pmatrix} \delta\mathbf{u}_f \\ \mathbf{0} \end{pmatrix}. \tag{20}$$

In every iteration, the sliding displacements may only be altered for sliding mechanisms which are found to be active: i.e., for which the sliding criterion $\phi = 0$ is met. How this sliding activity is determined is discussed below; for now we consider it as given. Hence, a distinction between active mechanisms (subscript a) and passive mechanisms (subscript p) is made. By partitioning Eq. (16) according to this distinction, it can be reformulated as:

$$\phi_a = \mathbf{0}, \quad \dot{\xi}_a \geqslant \mathbf{0}$$

$$\phi_p < \mathbf{0}, \quad \dot{\xi}_p = \mathbf{0}. \tag{21}$$

This set of equations shows that an equality constraint applies to each sliding mechanism, either in terms of ϕ_a or ξ_p. These constraints will be used to determine the iterative correction of the sliding displacements $\delta\mathbf{s}$. To this end, $\delta\mathbf{s}$ is also partitioned according to sliding activity. Since the passive sliders $\mathbf{s}_p$ must remain constant, $\delta\mathbf{s}_p = \mathbf{0}$. Hence, the sliding displacement correction $\delta\mathbf{s}$ can be formulated as:

$$\delta\mathbf{s} = \begin{pmatrix} \delta\mathbf{s}_a \\ \delta\mathbf{s}_p \end{pmatrix} = \begin{pmatrix} \delta\mathbf{s}_a \\ \mathbf{0} \end{pmatrix}. \tag{22}$$

On the basis of these distinctions, the linearized expressions for the force changes (see Eq. (17)) can be partitioned. The details of this process are given in Appendix A. Using the resulting expressions, a solvable system can be formulated by specifying the force changes $\delta\mathbf{F}_{u,f}$ and $\delta\mathbf{F}_{s,a}$. Eq. (4) dictates that the nodal force residual $\mathbf{F}_u - \mathbf{F}_{ext}$ should be reduced to zero, such that $\delta\mathbf{F}_{u,f} = \mathbf{F}_{ext,f} - \mathbf{F}_{u,f}$, where $\mathbf{F}_{u,f}$ are the values obtained in the previous iteration. Furthermore, to satisfy $\phi_a = \mathbf{0}$, the magnitudes of the driving forces for the active sliding mechanisms should be reduced to the critical level in the direction of the forces, such that $\delta\mathbf{F}_{s,a} = -(|\mathbf{F}_{s,a}| - \mathbf{F}_{sc,a}) * \text{sign}(\mathbf{F}_{s,a})$. Substitution of these expressions in the partitioned linearized system (see Eq. (A.4) in Appendix A) allows one to formulate this system as:

$$\mathbf{K}_{uu,ff}\delta\mathbf{u}_f + \mathbf{K}_{us,fa}\delta\mathbf{s}_a = \mathbf{F}_{ext,f} - \mathbf{F}_{u,f},$$

$$\mathbf{K}_{su,af}\delta\mathbf{u}_f + \mathbf{K}_{ss,aa}\delta\mathbf{s}_a = -(|\mathbf{F}_{s,a}| - \mathbf{F}_{sc,a}) * \text{sign}(\mathbf{F}_{s,a}). \tag{23}$$

By solving these coupled systems of equations and substituting the obtained corrections $\delta\mathbf{u}_f$ and $\delta\mathbf{s}_a$ in Eqs. (20) and (22) respectively, the iterative displacement corrections $\delta\mathbf{u}$ and $\delta\mathbf{s}$ are found. Subsequently, the variables $\mathbf{u}$ and $\mathbf{s}$ can be updated according to:

$$\mathbf{u} = \mathbf{u} + \delta\mathbf{u}$$

$$\mathbf{s} = \mathbf{s} + \delta\mathbf{s}, \tag{24}$$

and the forces $\mathbf{F}_u$ and $\mathbf{F}_s$ may be computed. This process is repeated until convergence is reached.

3.3. Active set strategy

Fluctuations in $\mathbf{F}_s$ may necessitate an update of the active set (i.e., the set of sliding mechanisms that are active) in every iteration. This update consists of checks for activation and deactivation, which are discussed below. Since these checks are done for each sliding mechanism individually, we focus on an individual sliding mechanism and drop its index i for ease of notation.

An essential part of the active set update is the possibility of sliding mechanism activation. A characteristic of every passive sliding mechanism is that it satisfies $\phi < 0$ as dictated by Eq. (21). A sliding mechanism is activated if it no longer satisfies this condition. As a consequence, its sliding displacement may be changed to prevent the magnitude of the sliding force from violating the threshold in the following iterations.

As a validation of every active sliding mechanism, it is evaluated if, according to Eq. (14), $\text{sign}(F_s) = \text{sign}(\Delta s)$, where $\Delta s = s - s^{(t)}$ is the incremental correction of s so far. Once an active sliding mechanism is found to violate this requirement, it is removed from the active set and thus becomes passive. Since its iterative sliding displacement value s is unreliable in this case, its value is reset to that at time $t : s := s^{(t)}$. The iteration process is then continued with $s = s^{(t)}$ for the following iteration.

In the first iteration of each increment, the last known sliding activity of the previous time increment is used as an initial estimate. In this manner, the incremental solution is found in a single iteration if no change in sliding activity occurs. This is efficient if small time steps are used. Furthermore, multiple sliding mechanisms may in principle be (de) activated simultaneously in one iteration. It is therefore important that the incremental loading steps are sufficiently small to prevent multiple sliding mechanisms from being activated and afterwards deactivated simultaneously.

4. Results

This section illustrates the capabilities of the proposed framework for a straightforward discrete network; an X-braced lattice. It serves to provide better insight into how the mechanical aspects modelled on the microscale, especially fiber sliding, affect the macroscopic mechanical response. The influence of various parameters is investigated for this purpose.

4.1. Problem description

A two-dimensional lattice of 16×16 nodes is subjected to a tensile deformation (see Fig. 3). The lattice is characterized by a square X-braced unit cell, with nodes present only at locations where horizontal, vertical and diagonal elements cross each other. Consequently, four fibers (chains of elements) pass through each node. We have found this to be the smallest number of characteristic directions in the network for which realistic degrees of anisotropy are still obtained, even in elastic networks. If more fiber directions would be included, that are all connected to each node, this might lead to an overly stiff response. The undeformed length of the vertical and horizontal springs is l_0, such that the unit cell has dimensions $l_0 \times l_0$. The entire network has a size $L_0 \times L_0$, with $L_0 = 15l_0$. For smaller lattices boundary effects are expected to strongly dominate the mechanics, whereas much larger networks require excessive computational expenses.

Inspired by most real fibrous materials, e.g., as treated by Ridruejo et al. (2010), the fibers in the network are given a finite length (see Fig. 3). Moreover, this introduces disorder in the lattice, which
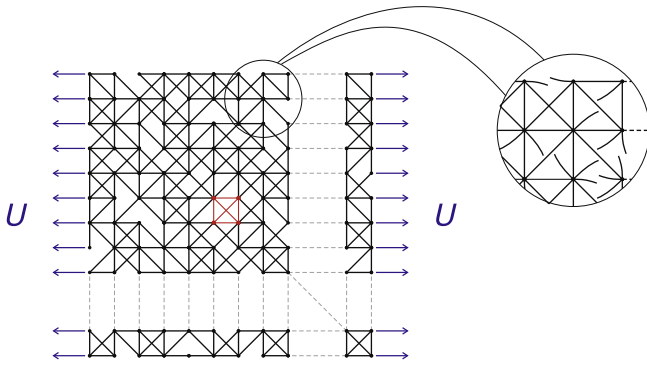
Fig. 3. Illustration of the lattice characterized by a square X-braced unit cell, cut to finite fibers of length $e_f = 4$ elements. No nodes are present at the locations where only the diagonal elements cross each other. A horizontal displacement U in outward directions is imposed to the nodes on the vertical edges. The fibers are assumed to have free ends, as illustrated on the right.

Fig. 4. The normalized horizontal reaction force ($F/(kl_0)$) as a function of the normalized imposed displacement (U/l_0) for the reference situation (solid) and the purely elastic case (dashed).

reduces the influence of boundary effects. In the following, fibers consist of straight chains of a constant number of elements e_f. In the reference case, $e_f = 4$, as in Fig. 3. To implement the uniform fiber length in the lattice, one element is first removed from every straight chain of elements at a randomly chosen position. This simulates a first 'cut', since the two free fiber ends formed by a cut cannot transfer load. Along the remainder of the chain of elements, every $(e_f + 1)$th element away from the first cut is also removed to divide the element chain into finite fibers of e_f elements (or less near the boundaries). Instead of actually removing an element, its stiffness is set to a small nonzero value (10^{-5} times its original stiffness) to promote computational stability.

The tensile tests are performed quasi-statically, by imposing a monotonically increasing displacement, U, to the nodes on the vertical edges of the network. The vertical displacement of these nodes is restricted. As a result, the nodes in the lattice are displaced (described by **u**) and fibers may slide through the nodes (described by **s**). Four principal fiber orientations are distinguished in the lattice (i.e., one horizontal, one vertical and two diagonal), such that four sliding mechanisms are present in each node. No sliding is allowed in the nodes on the vertical edges, such that the displacement U imposed on these nodes is effectively transferred to the rest of the lattice.

The increments of imposed displacement ΔU are small compared to l_0. To obtain the results presented below, $\Delta U = l_0/1600$ is used in each simulation. Smaller increments do not significantly affect the results, whereas larger increments may lead to inaccurate results or may even cause the solution algorithm to fail to converge.

For the sake of simplicity, all springs have the same stiffness k (thus, also the diagonal springs). A distribution of bond strengths (or critical sliding forces) is used (i.e., the values in $\mathbf{F}_{sc}$ are not the same) to avoid singularities. The bond strengths are randomly selected from a uniform distribution around the mean bond strength $\overline{F}_{sc}$ with an interval $((1 - \eta)\overline{F}_{sc}, (1 + \eta)\overline{F}_{sc})$. Here, η characterizes the scatter of the bond strengths ($0 < \eta < 1$).

In the tensile testing of fibrous materials, fiber pullout plays a role in the failure process (Isaksson et al., 2006). The numerical networks studied here are assumed to be loaded up to a point where pullout has not occurred yet, by assuming that free fiber ends are sufficiently long to maintain the initial interfiber connection (see Fig. 3). Fibers are also assumed to have long free ends outside the upper and lower edges of the network, such that vertical or diagonal sliding may occur through the nodes at these edges.

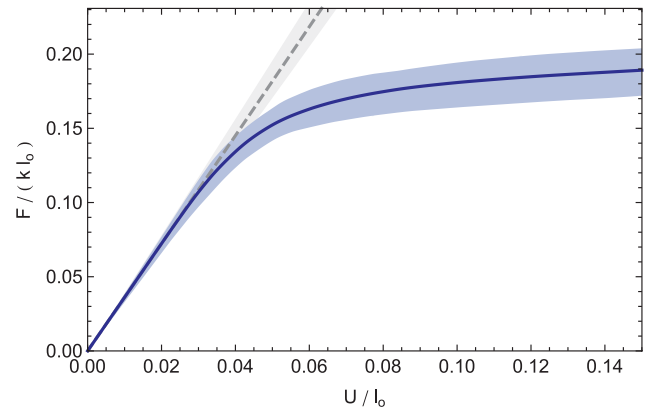Each result shown below is based on seven simulations, unless indicated otherwise. The simulations have varying lattice connectivity, i.e., for every simulation a new geometry is generated by initiating the cutting of the fibers at random positions. This introduces scatter, which is visualized by a colored band that envelopes the results of all (seven) simulations. The solid line inside this band represents the mean result of these simulations.

4.2. Reference case

Let us first consider a reference set of mesoscopic parameter values, which are given as $\overline{F}_{sc} = kl_0/200$, $\eta = 0.1$ and $e_f = 4$. Fig. 4 shows the evolution of the sum of the horizontal reaction forces, F, as a function of the imposed displacement U for these parameters. The two quantities are normalized to the stiffness and length of a single horizontal element. The elastic responses of the same networks are also shown for comparison.

The diagram shows that for relatively small displacements, the response is purely elastic and thus is solely governed by fiber stretching. The linear elasticity of the modelled fibers renders the force–displacement relation linear for small displacements U. As the imposed displacement increases, the response gradually starts to deviate from the elastic response and is eventually dominated by inelastic fiber sliding. This result qualitatively compares well with experimentally found force–displacement curves of a variety of fibrous materials (Niskanen, 1998; Bronkhorst, 2003; Beex and Peerlings, 2009; Ridruejo et al., 2010, 2011).

The band with scatter relative to the mean values of F observed in Fig. 4 appears to be approximately constant. From this it can be concluded that this scatter is primarily induced by geometric variations rather than variations in F_{sc}.

The transition from elastic to plastic deformation witnessed in Fig. 4 is further illustrated by Fig. 5. This figure shows the total work performed on the system, W, (which is the supplied energy by the imposed displacement U), the elastic energy stored in the lattice, E, and the accumulated amount of dissipation, D, (which is the energy dissipated by all sliding displacements) as functions of the imposed displacement, U. Fig. 5 shows that the initial response is governed by the buildup of elastic energy in the discrete elements. From the yield point onwards ($U \approx 0.025l_0$), energy is increasingly dissipated by friction in the fiber-node connections, which is responsible for the plasticity witnessed in Fig. 4. At the end of the deformation process (at $U \approx 0.14l_0$), the stored energy tends to stagnate and almost all supplied energy is dissipated by friction. The fact that the stored energy still slightly increases indicates that element straining plays a role in the slight hardening witnessed in this regime in Fig. 4. Note that Fig. 5 shows that the
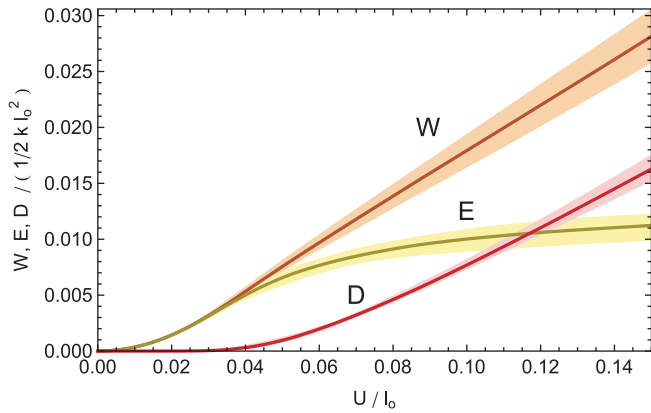
Fig. 5. The normalized total work performed by the system W, the normalized elastic energy stored in the lattice E and the normalized accumulated amount of total dissipation D, all normalized by $\frac{1}{2}kl_0^2$, as functions of the normalized imposed displacement (U/l_0).

first and second laws of thermodynamics are obeyed, since $W = E + D$ (which is consistent with $P_{ext} = \dot{E} + \dot{D}$) and $\dot{D} \geqslant 0$.

The distribution of sliding activity over the nodes for four of the seven simulations (arbitrarily chosen) is illustrated in Fig. 6. It shows that for the plasticity-dominated response at $U = 0.125l_0$,
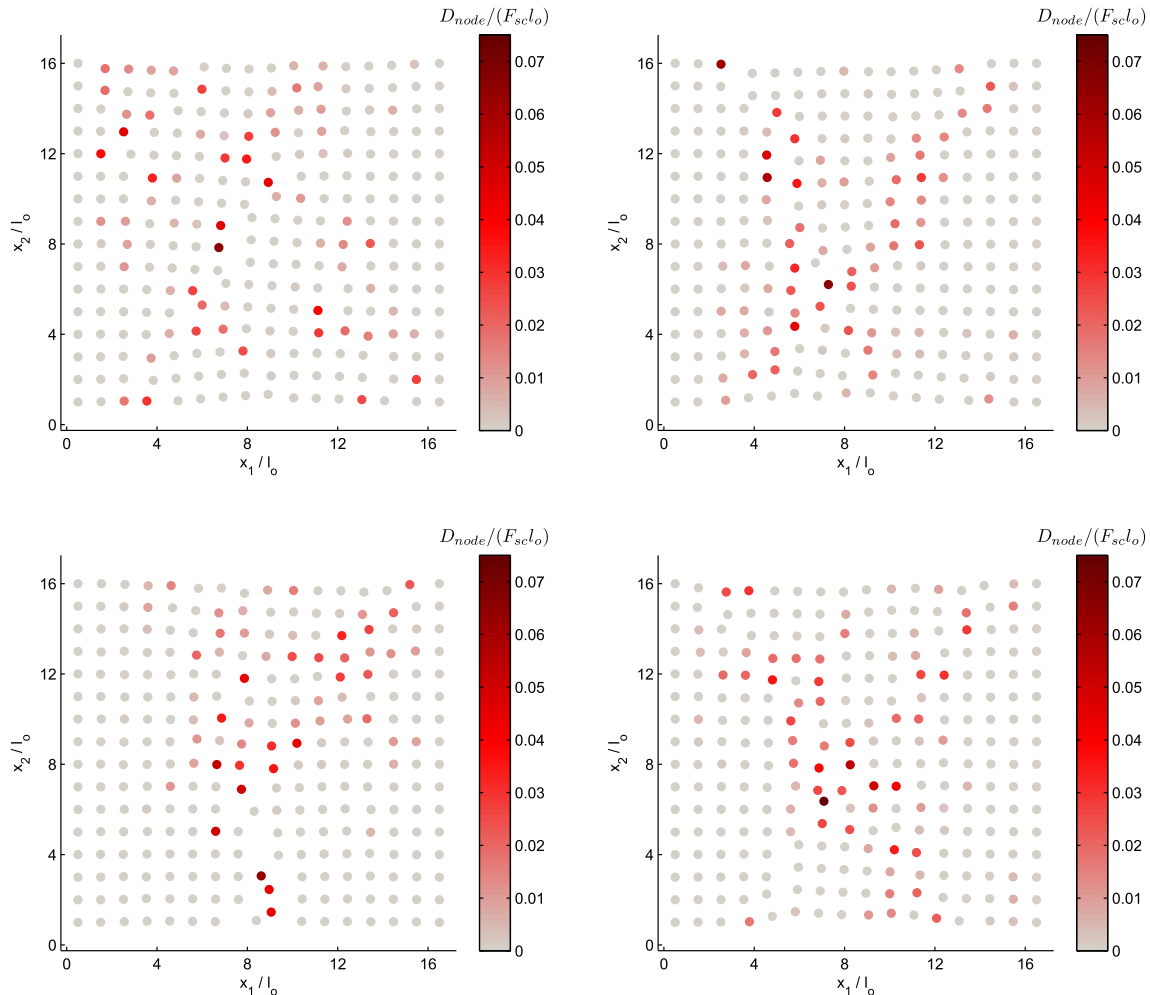
dissipation has localized into a number of nodes, whereas no dissipation has occurred in the majority of nodes. The dissipation appears to be more or less localized in a band that runs between the upper and lower edges of the specimen. The deformation of the network, which is also shown, is consistent with this localization band. Similar localization bands can also be observed in the results of Ridruejo et al. (2010) and Kulachenko and Uesaka (2012).

It appears that no consistent pattern can be identified in the dissipation localization, except that the localization bands are generally oriented perpendicular to the loading direction. This inconsistency is induced by both the geometric variations and the variations in the values of $\mathbf{F}_{sc}$. Two boundary layers in which hardly any sliding occurs are consistently observed along the vertical edges of the network.

Fig. 7 shows the mean force–displacement curve of the reference case for cyclic loading (one strain cycle). It is clear that the unloading is initially elastic and takes place along approximately the initial loading stiffness. This is similar to the behaviour of continuum-based elastoplasticity models and in agreement with the unloading behaviour of fibrous materials such as paper (Thakkar et al., 2009). Under a continued decrease of the imposed displacement, an elastoplastic response is found in compression. Plastic yielding (i.e., fiber sliding) however occurs at a (compressive) stress which is substantially lower than the initial yield strength, indicating a strong Bauschinger effect (kinematic hardening). This is due to the elastic energy stored in the system, which helps to
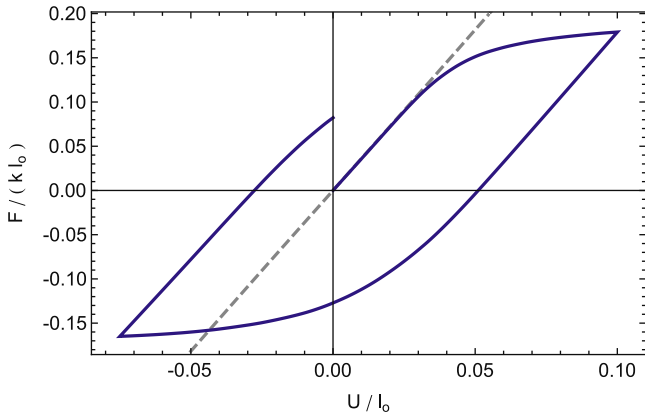

Fig. 6. Node-wise amount of energy dissipated by sliding at $U = 0.125l_0$ for four of the seven simulations, shown on the deformed geometry (displacements are scaled by a factor 4 in each direction for clarity).

Fig. 7. The normalized mean horizontal reaction force ($F/(kl_0)$) as a function of the normalized imposed displacement (U/l_0) which is increased from $U = 0$ to $U = 0.1l_0$, then decreased to $U = -0.075l_0$ and increased again to $U = 0$ for the reference situation (solid). The purely elastic response is shown by the dashed curve.

Fig. 9. The normalized horizontal reaction force ($F/(kl_0)$) as a function of the normalized imposed displacement (U/l_0) for three finite fiber lengths (e_f). The curve of the reference case is indicated by $e_f = 4$ and the purely elastic response of the reference case is shown by the dashed curve.

overcome the friction resistance upon reverse loading. Note that a similar effect occurs upon renewed tensile loading.

4.3. Parameter study

To study the influence of the mean bond strength $\overline{F}_{sc}$, the simulations are repeated using half the reference value of $\overline{F}_{sc}$ and twice the reference value, while η is kept constant. Fig. 8 shows a comparison of the force–displacement curves for the three situations. Each set of simulations is stopped when the slope is 7% of the original stiffness. It is clear that the yield point is increased with increasing $\overline{F}_{sc}$. The strength (i.e., the reaction force for which the response is purely governed by sliding) appears to be proportional to $\overline{F}_{sc}$. This is expected, since $\overline{F}_{sc}$ quantitatively controls the sliding forces for which the response is sliding-dominated. The range in U over which the elastic–plastic transition takes place in Fig. 8 increases approximately linearly with the ultimate strength, since the scatter (characterized by η) is relative to $\overline{F}_{sc}$. This implies that the absolute width of the distribution that determines $\mathbf{F}_{sc}$ scales with $\overline{F}_{sc}$.

The influence of the fiber length e_f (measured in element lengths) is illustrated in Fig. 9. This diagram shows that the elastic network stiffness increases with the fiber length. The network strength also increases with the fiber length. It approximately doubles upon doubling the fiber length. It can also be observed that for
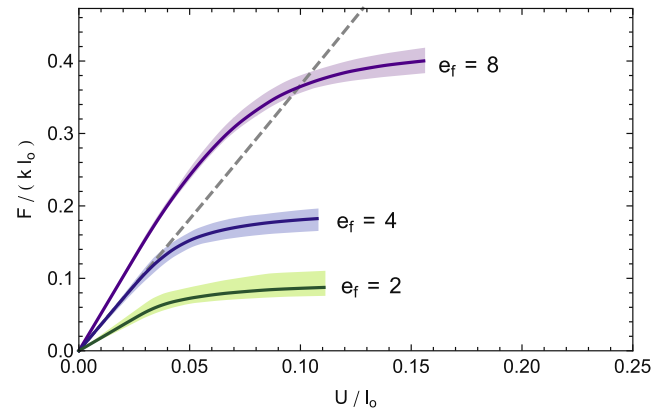
an increasing fiber length, the transition from elastic-dominated to plastic-dominated deformation is more gradual. The elevated stiffness, elevated strength and less distinctive yield point are all explained by the higher level of connectivity in the network for larger fiber lengths. The level of scatter relative to the mean of the tensile curve decreases with an increase of the fiber length, since a higher level of connectivity reduces the effects of geometric variations on the macroscopic response.

Fibrous materials are often characterized by preferred fiber orientations leading to anisotropic material responses. Anisotropy can be captured in the considered lattice model straightforwardly by changing the unit cell's aspect ratio. In Fig. 10 the influence of the aspect ratio is shown for the response in horizontal direction. The dimensions of the unit cell are now defined as $l_{0,x} \times l_{0,y}$. Since the unit cell in the reference situation is square ($l_{0,x} = l_{0,y} = l_0$), its aspect ratio equals one. For the other situations $l_{0,x}$ is either increased or decreased by a factor 1.5, while $l_{0,y}$ and all other parameters have the same values as in the reference situation. Note that the horizontal and vertical axes in Fig. 10 have been normalized by $l_{0,x}$ and $l_{0,y}$ respectively. The figure shows that a higher aspect ratio corresponds to an increased relative (normalized) stiffness of the lattice in the horizontal direction (i.e., that of the long cell edge). This is explained by the smaller angle between the diagonal elements and the loading direction. For higher aspect ratios, the increased stiffness and identical yield forces result in a less gradual
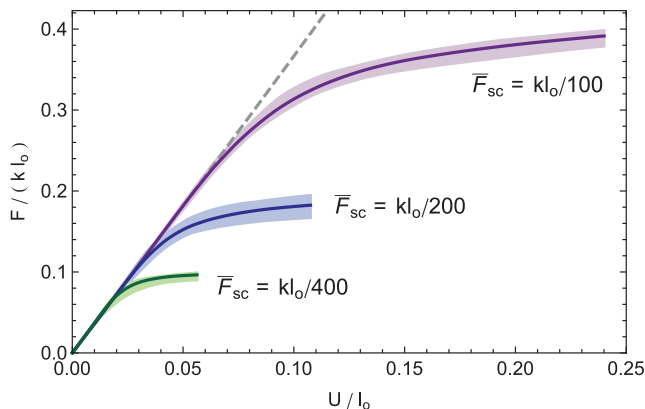

Fig. 8. The normalized reaction force ($F/(kl_0)$) as a function of the normalized imposed displacement (U/l_0) for three values of the normalized mean bond strength ($\overline{F}_{sc}/(kl_0)$). The curve of the reference case is indicated by $\overline{F}_{sc} = kl_0/200$ and the dashed curve shows the purely elastic response.
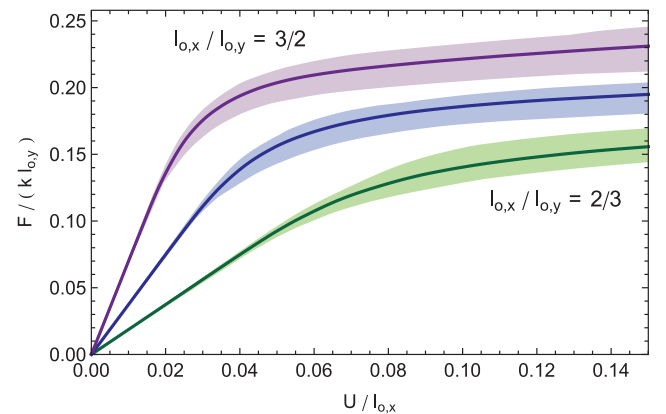

Fig. 10. The normalized horizontal reaction force ($F/(kl_{0,y})$) as a function of the normalized imposed displacement $U/l_{0,x}$ for three unit cell aspect ratios ($l_{0,x}/l_{0,y}$). The curve of the reference case is presented without an aspect ratio ($l_{0,x}/l_{0,y} = 1$).

transition from elastic to plastic lattice deformation. The vertical response (not shown here) exhibits the opposite trend, and the degree of anisotropy thus increases with the aspect ratio.

5. Concluding remarks

Interfiber bond failure and subsequent frictional fiber sliding are important aspects of the deformation process of several fibrous materials (Isaksson et al., 2006; Zhu et al., 2007; Ridruejo et al., 2010, 2011; Kulachenko and Uesaka, 2012). In this paper, interfiber bond failure in mesoscopic spring network models, followed by frictional fiber sliding, is incorporated in an isothermal thermodynamical setting. The model is applied to an X-braced lattice with finite fibers. Each finite fiber is modelled by a chain of elastic springs and the behaviour of the interfiber bonds is described by dry friction. However, the model can be adapted so that different network connectivities, element behaviours and bond descriptions (e.g., a viscoplastic description) can be studied. A framework to numerically approximate the nonlinear model for simulating lattice deformation is proposed as well. It is used to systematically investigate the influence of different mesoscopic parameters on the macroscopic response.

The results for the X-braced lattice with finite fibers illustrate that, with simple descriptions for fiber stretching and interfiber friction, the model exhibits an elastoplastic macroscopic response that mimics the macroscopic mechanical behaviour of several fibrous materials. Energy is dissipated due to localized fiber sliding, that is typically concentrated in a path across the network. The network model exhibits kinematic hardening under cyclic loading. It is furthermore shown that an increase of the fiber length leads to a stiffer macroscopic response, a higher macroscopic strength and a less pronounced macroscopic yield point. Finally, anisotropy is implemented by changing the aspect ratio of the unit cell. The results show an elevated stiffness and a less smooth transition from elastic to plastic deformation for an increasing aspect ratio.

The present model may serve as a basis for the construction of discrete network models that connect several key aspects of the deformation witnessed in fibrous materials. For instance, elastoplastic fibers (present in paper (Page and El-Hosseiny, 1983; Bronkhorst, 2003)) may enter the model through the thermodynamical setting. To capture the degradation of interfiber bond response under the influence of sliding (e.g., modelled by Ridruejo et al. (2010)) alternative relations for sliding can be incorporated. The brittle failure of fibers and bonds (e.g., modelled by Lilliu and Van Mier (2003), Bolander and Sukumar (2005), Liu et al. (2010) and Heyden (2000); Liu et al. (2010); Ridruejo et al. (2010), respectively) may be modelled by dictating thresholds for the corresponding forces. The ability of such network models to quantitatively reproduce experimental results using estimates of the model parameters remains a subject for further research.

Acknowledgements

Appendix A. Partitioning of the linearized system

The linearized system in Eq. (17) can be reformulated as:

$$\begin{pmatrix} \delta\mathbf{F}_u \\ \delta\mathbf{F}_s \end{pmatrix} = \begin{pmatrix} \mathbf{K}_{uu} & \mathbf{K}_{us} \\ \mathbf{K}_{su} & \mathbf{K}_{ss} \end{pmatrix} \begin{pmatrix} \delta\mathbf{u} \\ \delta\mathbf{s} \end{pmatrix}. \tag{A.1}$$

Partitioning of this system of equations on the basis of the free-constrained and active–passive distinctions, as explained in Section 3.2, results in:

$$\begin{pmatrix} \delta\mathbf{F}_{u,f} \\ \delta\mathbf{F}_{u,c} \\ \delta\mathbf{F}_{s,a} \\ \delta\mathbf{F}_{s,p} \end{pmatrix} = \begin{pmatrix} \mathbf{K}_{uu,ff} & \mathbf{K}_{uu,fc} & \mathbf{K}_{us,fa} & \mathbf{K}_{us,fp} \\ \mathbf{K}_{uu,cf} & \mathbf{K}_{uu,cc} & \mathbf{K}_{us,ca} & \mathbf{K}_{us,cp} \\ \mathbf{K}_{su,af} & \mathbf{K}_{su,ac} & \mathbf{K}_{ss,aa} & \mathbf{K}_{ss,ap} \\ \mathbf{K}_{su,pf} & \mathbf{K}_{su,pc} & \mathbf{K}_{ss,pa} & \mathbf{K}_{ss,pp} \end{pmatrix} \begin{pmatrix} \delta\mathbf{u}_f \\ \delta\mathbf{u}_c \\ \delta\mathbf{s}_a \\ \delta\mathbf{s}_p \end{pmatrix}. \tag{A.2}$$

By using $\delta\mathbf{u}_c = \mathbf{0}$ and $\delta\mathbf{s}_p = \mathbf{0}$, this system can be simplified to:

$$\begin{pmatrix} \delta\mathbf{F}_{u,f} \\ \delta\mathbf{F}_{u,c} \\ \delta\mathbf{F}_{s,a} \\ \delta\mathbf{F}_{s,p} \end{pmatrix} = \begin{pmatrix} \mathbf{K}_{uu,ff} & \mathbf{K}_{us,fa} \\ \mathbf{K}_{uu,cf} & \mathbf{K}_{us,ca} \\ \mathbf{K}_{su,af} & \mathbf{K}_{ss,aa} \\ \mathbf{K}_{su,pf} & \mathbf{K}_{ss,pa} \end{pmatrix} \begin{pmatrix} \delta\mathbf{u}_f \\ \delta\mathbf{s}_a \end{pmatrix}. \tag{A.3}$$

The equations in this system that correspond to $\delta\mathbf{u}_c$ and $\delta\mathbf{s}_p$ (the second and fourth equations) are left out of consideration. This can be done since the solution $\delta\mathbf{u}_f$ and $\delta\mathbf{s}_a$ is found by specifying the terms $\delta\mathbf{F}_{u,f}$ and $\delta\mathbf{F}_{s,a}$ and solving the first and third equations of this system. These equations can be reformulated as:

$$\delta\mathbf{F}_{u,f} = \mathbf{K}_{uu,ff}\delta\mathbf{u}_f + \mathbf{K}_{us,fa}\delta\mathbf{s}_a$$
$$\delta\mathbf{F}_{s,a} = \mathbf{K}_{su,af}\delta\mathbf{u}_f + \mathbf{K}_{ss,aa}\delta\mathbf{s}_a. \tag{A.4}$$

References

Abadie, J., Carpentier, J., 1969. Generalization of the Wolfe reduced gradient method to the case of nonlinear constraints, Optimization. Academic Press, New York, United States, 37–49.

Alava, J., Duxbury, J., 1996, Disorder-induced roughening in the three-dimensional Ising model, Physical Review B, vol. 51, 14.990–14.993.

Arnoux, P.J., Bonnoit, J., Chabrand, P., Jean, M., Pithioux, M., 2002. Numerical damage models using a structural approach: application in bones and ligaments. The European Physical Journal of Applied Physics 17, 65–73.

Beex, L.A.A., Peerlings, R.H.J., 2009. An experimental and computational study of laminated paperboard creasing and folding. International Journal of Solids and Structures 46, 4192–4207.

Ben Boubaker, B., Haussy, B., Ganghoffer, J.F., 2007. Discrete models of woven structures. Macroscopic approach. Composites: Part B 38, 498–505.

Bolander, J.E., Sukumar, N., 2005. Irregular lattice model for quasistatic crack propagation. Physical Review B 71, 094106.

Bronkhorst, C.A., 2003. Modelling paper as a two-dimensional elastic–plastic stochastic network. International Journal of Solids and Structures 40, 5441–5454.

Curtin, W.A., Scher, H., 1989. Brittle fracture in disordered materials: A spring network model. Journal of Materials Research 5, 3535–3553.

Delaplace, A., Pijaudier-Cabot, G., Roux, S., 1996. Progressive damage in discrete models and consequences on continuum modelling. Journal of the Mechanics and Physics of Solids 44, 99–136.

Germain, P., 1973. The method of virtual power in continuum mechanics. Part 2: microstructure. SIAM Journal on Applied Mathematics 25, 556–575.

Hatami-Marbini, H., Picu, R.C., 2009. An eigenstrain formulation for the prediction of elastic moduli of defective fiber networks. European Journal of Mechanics A/Solids 28, 305–316.

Hatami-Marbini, H., Shahsavari, A., Picu, R.C., 2013. Multiscale modeling of semiflexible random fibrous structures. Computer-Aided Design 45, 77–83.

Heegaard, J.H., Curnier, A., 1993. An augmented Lagrangian method for discrete large-slip contact problems. International Journal for Numerical Methods in Engineering 36, 569–593.

Herrmann, H.J., Roux, S., 1990. Statistical models for the fracture of disordered media. North Holland, Amsterdam, The Netherlands.

Heyden, S., 2000. Network modelling for the evaluation of mechanical properties of cellulose fibre fluff, Doctoral thesis. Lund University, Lund, Sweden.

Isaksson, P., Hägglund, R., 2007. Evolution of bond fractures in a randomly distributed fiber network. International Journal of Solids and Structures 44, 6135–6147.

Isaksson, P., Gradin, P.A., Kulachenko, A., 2006. The onset and progression of damage in isotropic paper sheets. International Journal of Solids and Structures 43, 713–726.

Kulachenko, A., Uesaka, T., 2012. Direct simulation of fiber network deformation and failure. Mechanics of Materials 51, 1–14.

Lilliu, G., Van Mier, J.G.M., 2003. 3D lattice type fracture model for concrete. Engineering Fracture Mechanics 70, 927–941.

Liu, J.X., Chen, Z.T., Li, K.C., 2010. A 2-D lattice model for simulating the failure of paper. Theoretical and Applied Fracture Mechanics 54, 1–10.

Niskanen, K., 1998. Paper physics. Fapet Oy, Helsinki, Finland.

Ostoja-Starzewski, M., 2002. Lattice models in micromechanics. Applied Mechanics Reviews 55, 35–60.

Page, D.H., El-Hosseiny, F., 1983. The mechanical properties of single wood pulp fibres. Part VI. Fibril angle and the shape of the stress–strain curve. Journal of Pulp and Paper Science 9, 99–100.

Potluri, P., Manan, A., 2007. Mechanics of non-orthogonally interlaced textile composites. Composites: Part A 38, 1216–1226.

Räisänen, V.I., Alava, M.J., Nieminen, R.M., 1997. Failure of planar lattice models. Journal of Applied Physics 82, 3747–3753.

Ridruejo, A., González, C., Llorca, J.L., 2010. Damage micromechanisms and notch sensitivity of glass-fiber non-woven felts: An experimental and numerical study. Journal of the Mechanics and Physics of Solids 58, 1628–1645.

Ridruejo, A., González, C., Llorca, J.L., 2011. Micromechanisms of deformation and fracture of polypropylene nonwoven fabrics. International Journal of Solids and Structures 48, 153–162.

Ridruejo, A., González, C., Llorca, J.L., 2012. Damage localization and failure locus under biaxial loading in glass-fiber nonwoven felts. Journal for Multiscale Computational Engineering 40, 425–440.

Schlangen, E., Van Mier, J.G.M., 1992. Experimental and numerical analysis of micromechanisms of fracture of cement-based composites. Cement Concrete Composites 14, 105–118.

Simo, J.C., Taylor, R.L., 1986. A return mapping algorithm for plane stress elastoplasticity. International Journal for Numerical Methods in Engineering 22, 649–670.

Thakkar, B.K., Gooren, L.G.J., Peerlings, R.H.J., Geers, M.G.D., 2009. Experimental and numerical investigation of creasing in corrugated paperboard. Philosophical Magazine 88, 3299–3310.

Zhu, B., Yu, T.X., Tao, X.M., 2007. Large deformation and slippage mechanism of plain woven composite in bias extension. Composites: Part A 38, 1821–1828.